

# Finite element simulations of the cyclic elastoplastic behaviour of copper thin films

Filip Šiška<sup>1</sup>, Samuel Forest<sup>1</sup>, Peter Gumbsch<sup>2,3</sup> and Daniel Weygand<sup>2</sup>

<sup>1</sup> Centre des Matériaux / Mines Paris, Paristech, CNRS UMR 7633, B.P. 87, 91003 Evry Cedex, France

<sup>2</sup> Institut für Zuverlässigkeit von Bauteilen und Systemen (izbs), Universität Karlsruhe, Kaiserstr. 12, 76131 Karlsruhe, Germany

<sup>3</sup> Fraunhofer-Institut für Werkstoffmechanik IWM / Wöhlerstr. 11, 79108 Freiburg, Germany

Received 3 July 2006, in final form 23 October 2006

Published 8 December 2006

Online at [stacks.iop.org/MSMSE/15/S217](http://stacks.iop.org/MSMSE/15/S217)

## Abstract

A large-scale computational and statistical strategy is presented to investigate the development of plastic strain heterogeneities and plasticity induced roughness at the free surface in multicrystalline films subjected to cyclic loading conditions, based on continuum crystal plasticity theory. The distribution of plastic strain in the grains and its evolution during cyclic straining are computed using the finite element method in films with different ratios of in-plane grain size and thickness, and as a function of grain orientation (grains with a  $\{111\}$  or a  $\{001\}$  plane parallel to the free surface and random orientations). Computations are made for 10 different realizations of aggregates containing 50 grains and one large aggregate with 225 grains. It is shown that overall cyclic hardening is accompanied by a significant increase in strain dispersion. The case of free-standing films is also addressed for comparison. The overall surface roughness is shown to saturate within 10 to 15 cycles. Plasticity induced roughness is due to the higher deformation of  $\{001\}$  and random grains and due to the sinking or rising at some grain boundaries.

(Some figures in this article are in colour only in the electronic version)

## 1. Introduction

Metal thin films play an important role in microelectronics systems. The mechanical properties of thin films significantly differ from bulk polycrystalline responses. They are related to film thickness, grain size and crystallographic orientations. Recent experiments with thin metallic films deposited on different substrates [1–3] have aroused a strong interest in the computational mechanics community. In particular the continuum crystal plasticity theory was resorted to in order to simulate the plastic deformation of columnar grains in aluminium multicrystalline strips in [4] and zinc coatings in [5]. The case of tensile and cyclic loading of films on a substrate was handled in [6] based on a von Mises plasticity model.

The aim of the present work is to develop a large-scale computational and statistical strategy to investigate the development of plastic strain heterogeneities and free surface roughness in multicrystalline films subjected to cyclic loading conditions, based on continuum crystal plasticity framework as shown for instance in [7]. Such large-scale finite element simulations for a description of heterogeneous plastic deformation was already carried out in the case of bulk polycrystalline aggregates under monotonic loading in [8] and for directionally solidified polycrystals with long columnar grains in [9]. A first application of this methodology was proposed in copper thin films under monotonic loading in [10], where the attention was focused on the texture effect on elastic and plastic strain incompatibilities. In the present work, the typical texture of copper films as in [1] is adopted. An important parameter of the study is the ratio  $d/h$  of in-plane grain size  $d$  and film thickness  $h$ . As a reference, the case of free-standing films is also addressed. Two different loading conditions are investigated and the results are presented at different levels: global stress–strain response, mean response of grains with similar textures components, mean response per grain and finally distribution of plastic strain inside the grains.

The first section is dedicated to the description of film morphology, texture, finite element mesh and boundary conditions. The question of representativity of the samples is addressed. The retained constitutive equations of standard crystal plasticity are recalled. In the second part, the heterogeneity of stress and strain in aggregates during cycling is presented and discussed from a global and local point of view. The third part focuses on the evaluation of the roughness of the free surface of the films induced by plastic deformation during cyclic loading.

The results are presented mainly in terms of equivalent stress and strain measures, defined by

$$\sigma_{\text{eq}} = \sqrt{\frac{3}{2} \boldsymbol{s} : \boldsymbol{s}}, \quad \varepsilon_{\text{eq}} = \sqrt{\frac{2}{3} \boldsymbol{\varepsilon} : \boldsymbol{\varepsilon}}, \quad (1)$$

where  $\boldsymbol{s}$  is the deviatoric part of the stress tensor  $\boldsymbol{\sigma}$ . The overall response of the material is characterized by volume average stress and strain tensors:

$$\langle \boldsymbol{\Sigma} \rangle = \frac{1}{V} \int \boldsymbol{\sigma} \, dV, \quad \langle \boldsymbol{E} \rangle = \frac{1}{V} \int \boldsymbol{\varepsilon} \, dV, \quad (2)$$

where  $V$  is the volume occupied by the film. The proposed statistical approach makes use of the ensemble averaging operator over  $n$  realizations of the microstructure:

$$\bar{\boldsymbol{\Sigma}} = \frac{1}{n} \sum_{i=1}^n \boldsymbol{\Sigma}^i, \quad \bar{\boldsymbol{E}} = \frac{1}{n} \sum_{i=1}^n \boldsymbol{E}^i, \quad (3)$$

where  $\boldsymbol{\Sigma}^i$  and  $\boldsymbol{E}^i$  denote the mean stress and strain for the volume  $V^i$  of film number  $i$ . The volume and ensemble average operators can be applied to other variables as well.

## 2. Computational method

### 2.1. Grain morphology and crystallographic texture

The free surface of the multicrystalline films considered in this work is represented by a 2D Voronoi tessellation [8]. The 3D grains are obtained by an extension of the image of the free surface orthogonally to the surface. This is a usual simplified representation of columnar grains in films and coatings, for which all grain boundaries are quasi-perpendicular to the substrate or free surface [4, 11]. The Voronoi tessellation uses initial points which are placed randomly in the plane. Most of the grains have 5 to 7 edges which correspond approximately to real columnar grain structures [12]. The Voronoi model however is a crude representation of real

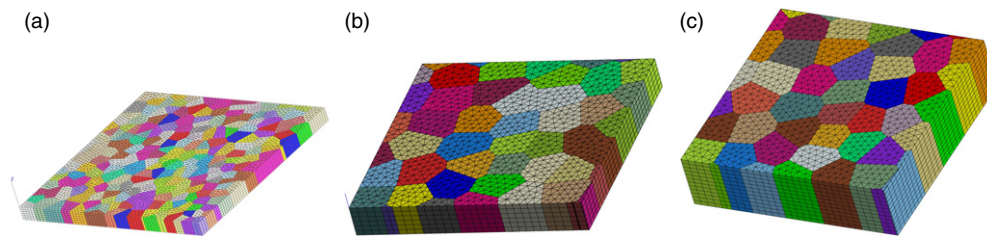


**Figure 1.** Morphology and finite element mesh of multicrystalline films: (a) 225-grain film with  $d/h = 1$ , (b) 50-grain film with  $d/h = 1$ , (c) 50-grain film with  $d/h = 0.5$ .

films made of columnar grains. This could be improved by a better morphological model based on the systematic EBSD measurement on metal films. In the first large-scale simulations of cyclic plasticity in films presented in this work, we have adopted this simplified microstructure. Future work should take a precise knowledge of the microstructure morphology into account. In particular, grain size distribution in real films is well described by the log normal distribution. The variation in the grain size of the simulated structure is smaller. Another limitation of this morphological model compared with actual copper films is the existence of numerous twins in grains that are not introduced in our model. Indeed, this should be incorporated in more realistic models, actually based on specific EBSD measurements from which the morphology of the twins and the corresponding relative orientations can be deduced and introduced in FE meshes. A first step in this direction was proposed in [13]. The presence of twins is expected to even increase the strain heterogeneity distribution studied in this work.

As a result, the microstructure is characterized by two characteristic lengths: in-plane grain size  $d$  and film thickness  $h$ . Only the ratio  $d/h$  plays a role in the computations reported in this work. This geometric ratio is characteristic for columnar grain structures in thin films. It is known that simulations based on classical continuum crystal plasticity are not sensitive to absolute size effects. Only the relative size effect  $d/h$  is accounted for. However, the effect of the absolute thickness of the copper films considered in this work is taken into account by the choice of the initial critical resolved shear stress  $\tau_0$  for slip (to be defined in section 2.3), which is taken here from scaling laws taken from the literature (Hall–Petch-like relationship). This remains a crude description of size effects in thin films. Simulations based on generalized continuum crystal plasticity modelling are planned in future work to improve the description of size effects [14].

The normal direction to the film is called  $z$  and corresponds to index 3 in index notation for tensors. Two orthogonal directions  $x$  and  $y$  (respective component index 1 and 2) are defined in the plane free surface, parallel to the edges of the rectangular surface.

Three different realizations of such multicrystalline aggregates are shown in figure 1. Figure 1(a) shows a film made of 225 columnar grains. Two films containing 50 grains each are presented in figures 1(b) and (c) for two different values of the ratio  $d/h$ . The case  $d/h = 1$  corresponds to equiaxed grains. In contrast, columnar grains with  $d/h = 0.5$  are elongated along the  $z$  axis.

The crystallographic orientations of the grains considered in this work correspond to the typical crystallographic texture of annealed copper films vapour deposited on a polyimide or silicon substrate [1]. Such textures are characterized by three main components.

- 90% of  $\{111\}$ -grains. In such grains, one  $\{111\}$  plane is parallel to the free surface. The orientation of the remaining in-plane crystal directions is a random variable with a uniform distribution.

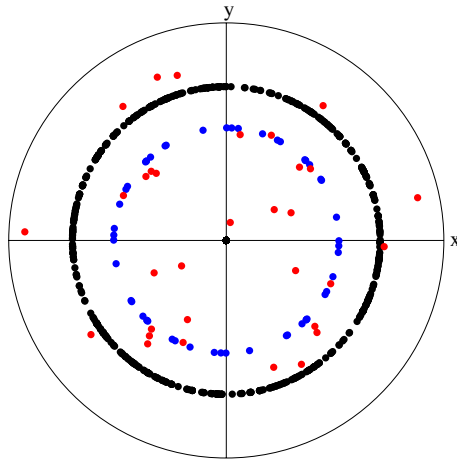


**Figure 2.** Pole figure  $[1\ 1\ 1]$  of the grain orientations in the 225-grain multicrystalline film of figure 1(a):  $\{1\ 1\ 1\}$ -grains in black,  $\{0\ 0\ 1\}$ -grains in blue, random grains in red.

- 6% of  $\{0\ 0\ 1\}$ -grains. In such grains, one  $\{0\ 0\ 1\}$  plane is parallel to the free surface. The orientation of the remaining in-plane crystal directions is a random variable with a uniform distribution.
- 4% of random grains.

Experimentally, there exist random slight deviations of  $[1\ 1\ 1]$  (respectively  $[0\ 0\ 1]$ ) crystal direction in  $\{1\ 1\ 1\}$ -grains (respectively  $\{0\ 0\ 1\}$ -grains) from the  $z$  axis. However, this scatter is not taken into account in this work. Ideal  $[1\ 1\ 1]$  or  $[0\ 0\ 1]$  orientations along  $z$  are attributed to the grains belonging to the two first texture components. The orientations of the grains used in the simulation of the 225-grain aggregate are given in the pole figure of figure 2. Ten realizations of 50-grain films were produced with grain orientations compatible with the described crystallographic texture on average. They are used for the simulations presented in this work.

## 2.2. Finite element mesh and boundary conditions

Standard 2D free meshing is used to obtain a finite element mesh of the free surface. A simple extension along  $z$  produces 3D prismatic elements as shown in figure 1. The elements are characterized by quadratic interpolation (15-node prisms) with reduced integration (6 Gauss integration points). The mesh size retained in this work is the following:

- the 225-grain FE mesh of figure 1(a) contains 47 000 elements and 136 000 nodes, i.e. 408 000 degrees of freedom (3 displacement components per node);
- the 50-grain FE mesh with  $d/h = 1$  of figure 1(b) contains 11 600 elements and 34 400 nodes, i.e. 103 200 degrees of freedom;
- the 50-grain FE mesh with  $d/h = 0.5$  of figure 1(c) contains 23 600 elements and 65 400 nodes, i.e. 196 200 degrees of freedom.

Two kinds of boundary conditions are used in the computations of this work to represent the following.

- *Free-standing films.* The faces of the parallelepipedic volume that are perpendicular to the  $z$  direction (or equivalently direction 3) are left free of forces, as shown in figure 3 case (a).

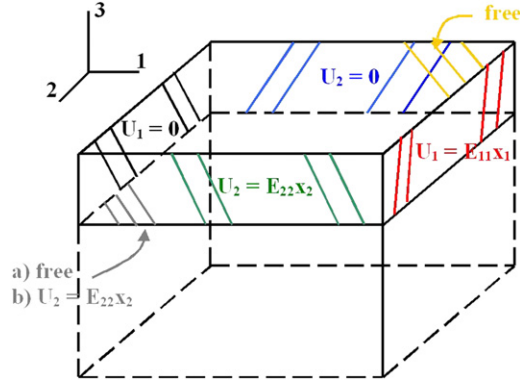


**Figure 3.** Boundary conditions used in the computation of free-standing films (a) and films on substrate (b). The deformation  $\underline{E}$  of the substrate is prescribed at the interface and on the lateral faces of the parallelepipedic volume.

Tensile loading is prescribed in direction  $y$  (or equivalently 2). For that purpose, the component  $U_2$  of the nodes belonging to the faces perpendicular to  $y$  is fixed to 0 at  $y = 0$  and increased linearly to a maximal value at  $y = L$ . Remaining boundary conditions aim at fixing rigid body motion.

- *Film on a substrate.* In addition to the previous boundary conditions, the nodes belonging to the face  $z = 0$  are subjected to homogeneous deformation:

$$U_i = E_{ij}^{\text{substrate}} x_j, \quad (4)$$

where the  $E_{ij}^{\text{substrate}}$  are the strain components of the substrate subjected to given simple tension, assuming that it deforms homogeneously (see case (b) at figure 3). As a result of this simplification, there is no meshing of the substrate. It is assumed that the overall strain of the substrate is homogeneously transmitted to the interface. The displacement component normal to each lateral face of the film is prescribed according to formula (4).

### 2.3. Constitutive equations

The constitutive model initially proposed in [15] and used for bulk copper bicrystals in [16] has been applied to copper thin films subjected to monotonic overall tensile loading in [10]. The constitutive equations are briefly recalled here within the small strain framework relevant for the applications presented in this work. Total strain is partitioned into elastic and plastic contribution, the elastic strain being related to stress via Hooke's law:

$$\underline{\varepsilon} = \underline{\varepsilon}^e + \underline{\varepsilon}^p, \quad \underline{\sigma} = \underline{\underline{C}} : \underline{\varepsilon}^e, \quad (5)$$

where  $\underline{\underline{C}}$  denotes the four rank tensor of elastic moduli. Plastic flow is the result of slip processes on 12 slip systems involving slip plane  $\underline{n}^s \in \{1\ 1\ 1\}$  and slip direction  $\underline{m}^s \in \langle 1\ 1\ 0 \rangle$ :

$$\dot{\underline{\varepsilon}}^p = \sum_{s=1}^{12} \dot{\gamma}^s \frac{1}{2} (\underline{n}^s \otimes \underline{m}^s + \underline{m}^s \otimes \underline{n}^s), \quad (6)$$

where  $\dot{\gamma}^s$  is the amount of slip for each slip system. Its evolution is given by

$$\dot{\gamma}^s = \left\langle \frac{|\tau^s - x^s| - r^s}{k} \right\rangle^n \text{sign}(\tau^s - x^s), \quad (7)$$

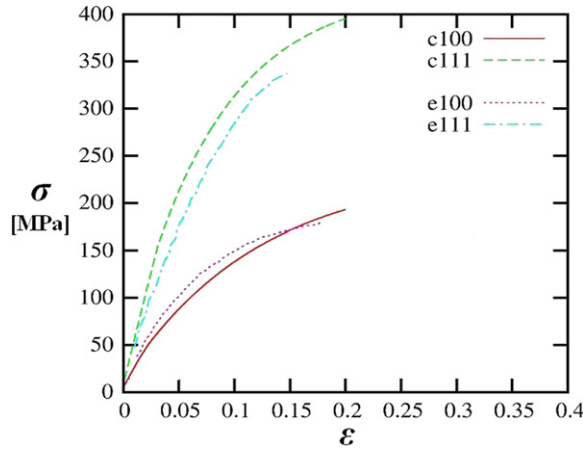


**Figure 4.** Comparison of experimental data (after [19]) and simulated curves for tensile tests of single crystal for different orientations: e—experiment, c—computation.

where  $\tau^s = \underline{m}^s \cdot \underline{\sigma} \cdot \underline{n}^s$  is the resolved shear stress on slip system  $s$ , according to the Schmid law. Coefficients  $k$  and  $n$  are viscosity parameters. The variables  $r^s$  and  $x^s$  are associated with isotropic and kinematic hardening, respectively. The nonlinear evolution rules for these hardening variables are

$$r^s = r_0 + q \sum_{r=1}^n h^{sr} (1 - \exp(-bv^r)), \quad \dot{v}^s = |\dot{\gamma}^s|, \quad (8)$$

$$x^s = c\alpha^s, \quad \dot{\alpha}^s = \dot{\gamma}^s - d\dot{v}^s\alpha^s, \quad (9)$$

where  $r_0$  is the initial critical resolved shear stress and  $h^{sr}$  is the interaction matrix. This matrix describes the self and latent hardening which is caused by interactions between different slip systems. The equation for kinematic hardening contains a linear contribution and a dynamic recovery term. Kinematic hardening represents in a purely phenomenological way the build-up of internal stresses (back-stress) induced by the forward and backward motion of dislocations in the material during cyclic loading. The existence of a back-stress in continuum single crystal modelling was motivated in [17, 18]. Two sets of parameters are used in the simulations presented in this work.

- *Isotropic hardening crystal plasticity model.* Only the isotropic hardening variable  $r^s$  is present in the model. The corresponding parameters were identified from the tensile tests on single crystals with various orientations from [19]. Experimental and simulated curves are in satisfactory agreement as shown in figure 4.
- *Kinematic hardening crystal plasticity model.* Both isotropic kinematic and isotropic hardening are included, which is especially relevant for cyclic behaviour. The material parameters are taken from [16] and calibrated from stress–strain loops for copper single and bicrystals where significant kinematic hardening was observed.

The results obtained with both models will be compared in order to isolate the contribution of internal stresses. Elastic behaviour is described by cubic elasticity. The parameters corresponding to both models are given in table 1. Note in particular the high values of latent hardening parameters found in [16]. This is due to the dependence of the interaction matrix on the investigated plastic strain range: high strain values in [19] and low strain values

**Table 1.** Values of the parameters for the two considered material models.

$C_{11}$ (MPa)	$C_{12}$ (MPa)	$C_{44}$ (MPa)
159 300	122 000	81 000
Parameter	Isotropic hardening model	Kinematic hardening model
$k$ (MPa.s <sup>1/n</sup> )	2.0	5.0
$n$	15.0	10.0
$q$ (MPa)	7.96	6.0
$b$	3.49	15.0
$c$ (MPa)	—	4500.0
$d$	—	600.0
$h_1$	1.0	1.0
$h_2$	1.4	4.4
$h_3$	1.4	4.75
$h_4$	1.4	4.75
$h_5$	1.4	4.75
$h_6$	1.4	5.0

for fatigue in [16]. The grain size effect is introduced by setting the initial critical resolved shear stress  $\tau_0 = 35$  MPa according to the Hall–Petch relationship for 1  $\mu\text{m}$  grain size [1, 20].

#### 2.4. Mesh size effect

Computations with four different meshes of the same aggregate with different mesh density were performed to evaluate the influence of mesh size on the results. These meshes are, respectively, labelled: coarse (21 555 nodes), standard (34 710 nodes), middle (56 973 nodes) and fine (112 163 nodes). The film with substrate was subjected to 5 cycles of tension-compression  $E_{22} = \pm 0.005$ . Figure 5 shows the comparison of the distribution of equivalent plastic strain after 5 cycles for the fine (a) and standard (b) meshes. Quantitative comparison is provided in figure 5(c) for the displacement component  $U_3$  along a line made of grain boundaries connecting one lateral side to the other still on the free surface. Differences remain small. In particular the highly deformed zones are the same in both cases with close plastic strain values (less than 2% differences locally). The ‘standard’ mesh density was chosen in order to provide detailed plastic strain maps with limited computation time. This corresponds to 2125 degrees of freedom per grain on average.

#### 2.5. Representative volume element size

An important aspect in computations of multicrystalline aggregates is the determination of representative volume element size, i.e. a finite size allowing an accurate enough estimation of global properties. The statistical approach developed for bulk materials in [21] and applied to thin films in [10] is adopted in this work. Each film configuration is represented by 10 different realizations of the aggregate with 50 grains, similar to the realization of figures 1(b) and (c). Final estimations are obtained as an ensemble average of the results over all realizations. This approach is validated by comparison of the overall stress–strain curve with that of the large aggregate with 225 grains of figure 1(a) subjected to the same overall loading conditions. For each realization the volume averaged stress–strain curve is recorded. The ensemble averaged stress–strain curve over 10 realizations is then displayed in figure 6 with the corresponding dispersion indicated by bars. It can be compared with the volume average stress–strain curve obtained for the 225-grain aggregate. For given grain morphology and texture, the macroscopic

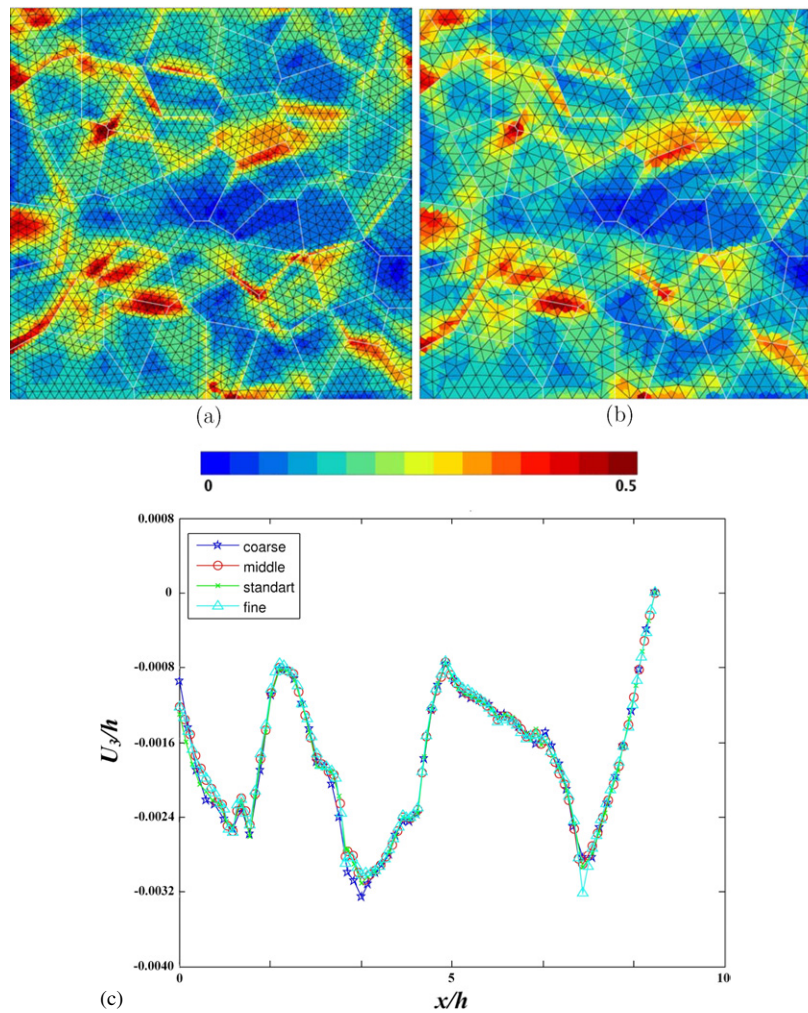


**Figure 5.** Cumulated plastic strain map for different mesh densities (cyclic tension-compression  $E_{22} = 0$ ,  $N = 5$ , scale in %): (a) fine mesh, (b) standart mesh (used in computations); grains boundaries are underlined in white; (c) quantitative comparison of displacement  $U_3$  along a line (made of grain boundaries linking the left edge to the right side on the free surface).

behaviour of small and large aggregates is very similar and therefore the proposed statistical approach is applicable.

### 3. Strain heterogeneities in cyclically deformed thin films

#### 3.1. Overall cyclic hardening

The multicrystalline films are subjected to two types of loading conditions:

- *cyclic tension-compression* with  $E_{22}^{\min, \max} = \pm 0.005$ , where  $E_{22}$  is the volume averaged axial deformation in the film. The prescribed mean strain rate is  $2 \times 10^{-6} \text{ s}^{-1}$ . For each realization of the microstructure, 100 cycles are simulated;
- *cyclic tension* with  $E_{22}^{\min, \max} = 0-0.005$  at the same mean strain rate.

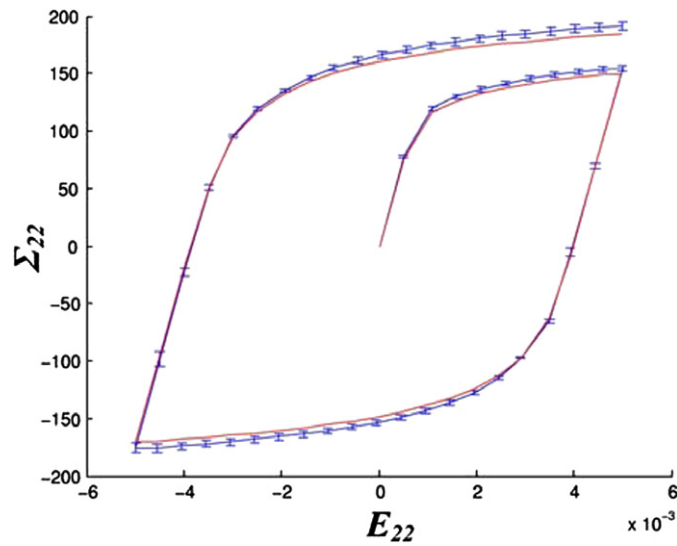


**Figure 6.** Overall stress–strain curve for the deformation of the 225-grain aggregate compared with the average overall curve with respect to 10 aggregates containing 50 grains each. The scatter in the response of the 50-grain aggregates is indicated by error-bars. The films are subjected to cyclic tension-compression  $E_{22}^{\min,\max} = \pm 0.005$ .

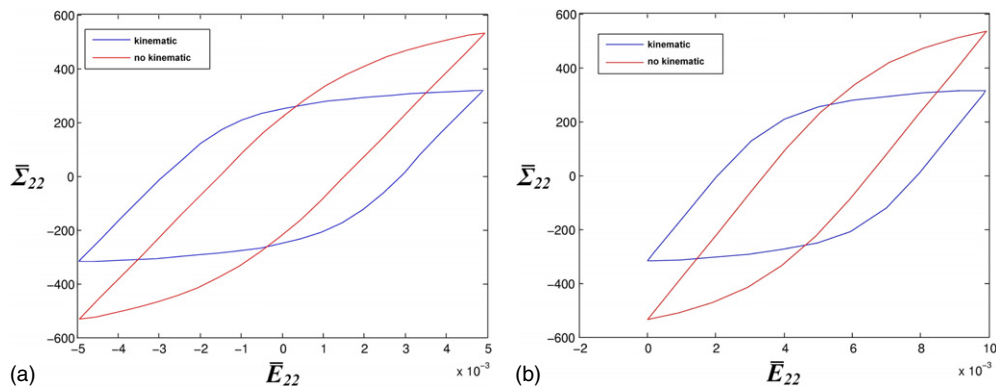


**Figure 7.** Stabilized overall stress–strain loops for models with and without local kinematic hardening (averaged over 10 realizations of 50-grain aggregates): (a) cyclic tension-compression, (b) cyclic tension.

The simulations are performed for 10 realizations for both loading conditions, for the two considered crystal plasticity models (with and without kinematic hardening) and for the three investigated film configurations (simple and double thickness, free-standing film). The evolution of mean stress and strain during cyclic loading is analysed. The stress–strain loops stabilize during cycling. The saturation loops are shown in figure 7 for both loading conditions and for both calibrated models. The stabilized maximal and minimal stress values are found to be almost identical for both loading conditions. This is due to total relaxation of mean stress during cyclic tension, which is a standard feature of low cycle bulk plasticity for non-symmetric strain loading conditions. No elastic accommodation takes place in the film for

cyclic tension tests. The stabilized loops predicted by both models are different. This is due to the fact that the isotropic hardening crystal plasticity was identified with respect to simple tension results on single crystals for larger strain ranges than in the present test. Only the results obtained with the kinematic hardening model will be analysed systematically in the next section because it was identified in the proper cyclic strain range. However, the simulation based on the isotropic hardening model shows that the interaction between grains in the film leads to an overall Bauschinger effect, clearly seen in figure 7. This is a known feature in bulk polycrystal plasticity [22]. The introduction of a back-stress in the single crystal model leads to a slightly stronger Bauschinger effect (blue curve in figure 7).

The comparison of stress–strain loops for the different texture components is shown in figure 8. For that purpose, the axial stress and strain components are volume averaged over all grains having a given orientation: all  $\{001\}$  grains, all  $\{111\}$  grains or all random orientations. The first and 100th loops are plotted for 5 realizations of aggregates with 50 grains. The grains with  $\{001\}$  and random orientations display significantly higher strain and lower stress levels than  $\{111\}$  ones. A higher dispersion of the loops is observed for  $\{001\}$  and random grains than for  $\{111\}$  grains, but this is due to the small number of such grains in aggregates: 3  $\{001\}$  grains and 2 random grains out of 50 for each realization. Complete stress relaxation is observed for all grain orientations in the case of cyclic tension so that the stabilized loops are symmetric in stress. The evolution with the number of cycles of the maximal value of stress averaged over all grains and realizations is shown in figure 9 for both loading conditions. The average stress level is stabilized after 70 cycles. The same saturation is observed for the mean stress for each texture component. The rate of saturation does not depend on the orientation group. The highest stress levels develop in  $\{111\}$  grains and the softest in  $\{001\}$  grains. These cyclic hardening curves result from volume and ensemble averaging over 450  $\{111\}$  grains, 30  $\{001\}$  grains and 20 random grains.

### 3.2. Levels of heterogeneity and statistical analysis

A first dispersion level of stress and strain was analysed in the previous section depending on the grain orientation group. A second dispersion level is given in figure 10 which shows the equivalent stress and strain value averaged over each individual grain in all realizations, after 100 cycles tension-compression (with substrate and  $d/h = 1$ ). A stress/strain concentration factor is defined as the ratio of the mean stress/strain in each grain divided by the overall stress/strain value for the corresponding aggregate. Stress concentration factors ranging mainly from 0.8 to 1.2 with extremal values of 0.6 and 1.6 are observed. The corresponding strain concentration factors range from 0.4 to 1.6. Low mean stresses are encountered mainly in  $\{001\}$  and random grains whereas high strain levels are found in grains belonging to all orientation groups.

The next dispersion level to be investigated is that of local stress and strain values inside the grains. The fields of equivalent plastic strain are shown in figure 11 at the free surface for three film configurations at the first and 100th cycle for cyclic tension-compression. In the simulations shown in figure 11, the grain morphology and crystal orientations are the same. Only the film configuration is changed (film thickness and substrate effect). Plastic strain is found to be highly heterogeneous with local values ranging from 0 (elastic response) to more than 0.01, i.e. twice the prescribed mean total strain. The plastic deformation develops into deformation bands inclined with respect to the vertical tensile axis and crossing several grains. Plastic strain is much more localized in these bands in free-standing films (figure 11(c)) than in films on a substrate. Plastic strain is more heterogeneous at the free surface in the thick film

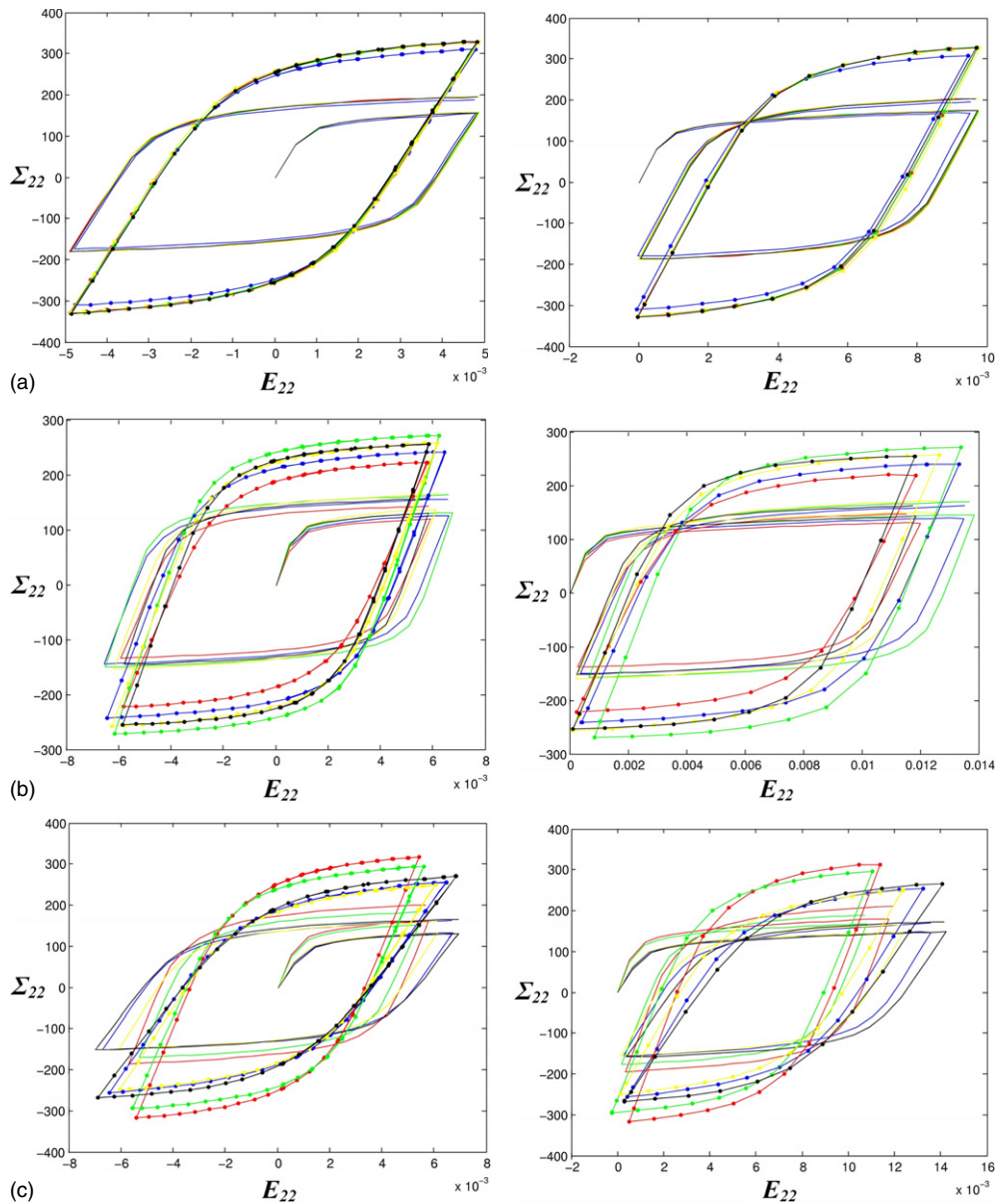


**Figure 8.** Comparison of first and stabilized cycles for different grain orientations in aggregates subjected to cyclic tension-compression (left) and cyclic tension (right): (a) volume average over  $\{111\}$  grains, (b) volume average over  $\{001\}$  grains, (c) volume average over random grains. In each case, the curves are given for 5 distinct realizations.

than in the twice thinner one (see figures 11(a) and (b)). Highly deformed grains are observed in figure 11(b), which is similar to the case of free-standing films.

For each film configuration, the comparison of the plastic strain map at the first and 100th cycle shows that the strain heterogeneities are more pronounced after 100 cycles, with, on the one hand, more localized deformation in some grains and close to some grain boundaries (red regions) and, on the other hand, more extended low strained zones (blue regions). A quantitative

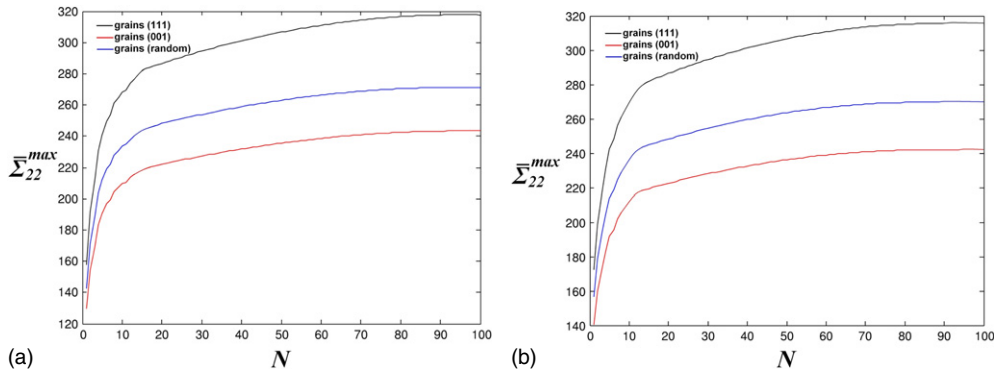


**Figure 9.** Cyclic hardening in multicrystalline aggregates subjected to (a) cyclic tension-compression, (b) cyclic tension. The overall stress curves are averaged over 10 realizations of 50-grain aggregates.

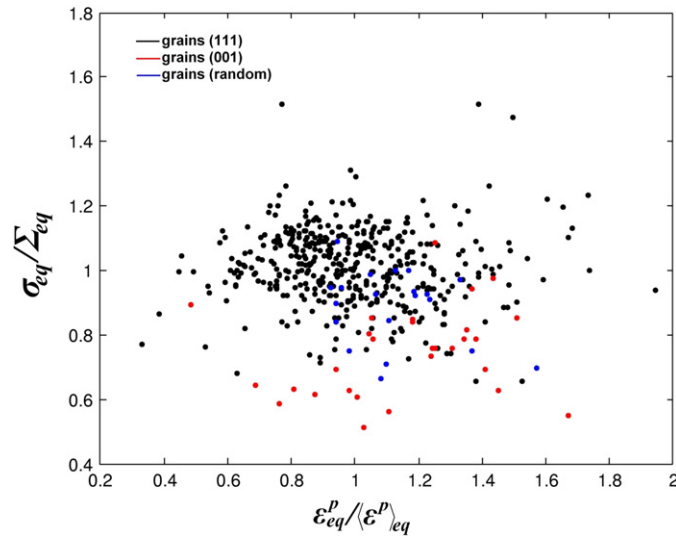


**Figure 10.** Dispersion of equivalent average stress and equivalent plastic strain in the grains of 10 realizations of 50-aggregates subjected to cyclic tension-compression at  $N = 100$ . The results are given for the films with a substrate with  $d/h = 1$ . Each point corresponds to the volume averaged stress value over one grain in the 10 aggregates. Black, blue and red dots, respectively, denote  $\{111\}$ ,  $\{001\}$  and random grains. The stress and plastic strain levels are normalized by the volume average values over the corresponding entire aggregate.

assessment of the evolution of heterogeneity distribution is possible via the following statistical analysis.

The plastic strain distribution in all the computed aggregates are represented by the histograms of figure 12. For each film configuration, the equivalent plastic strain values  $\varepsilon_{eq}^p$  at each integration point of each realization have been stored, normalized by the global value for the aggregate  $\langle\varepsilon^p\rangle_{eq}$  and ranked into classes of size  $\Delta\varepsilon_{eq}^p/\langle\varepsilon^p\rangle_{eq} = 0.1$ . The procedure was carried out for several cycle numbers:  $N = 1, 5, 50$ . Accordingly, each histogram represents the treatment of 696 000 values (corresponding to 10 realizations  $\times$  11 600 elements  $\times$  6 integration points per element for films with  $d/h = 1$ ). For each cycle number, three

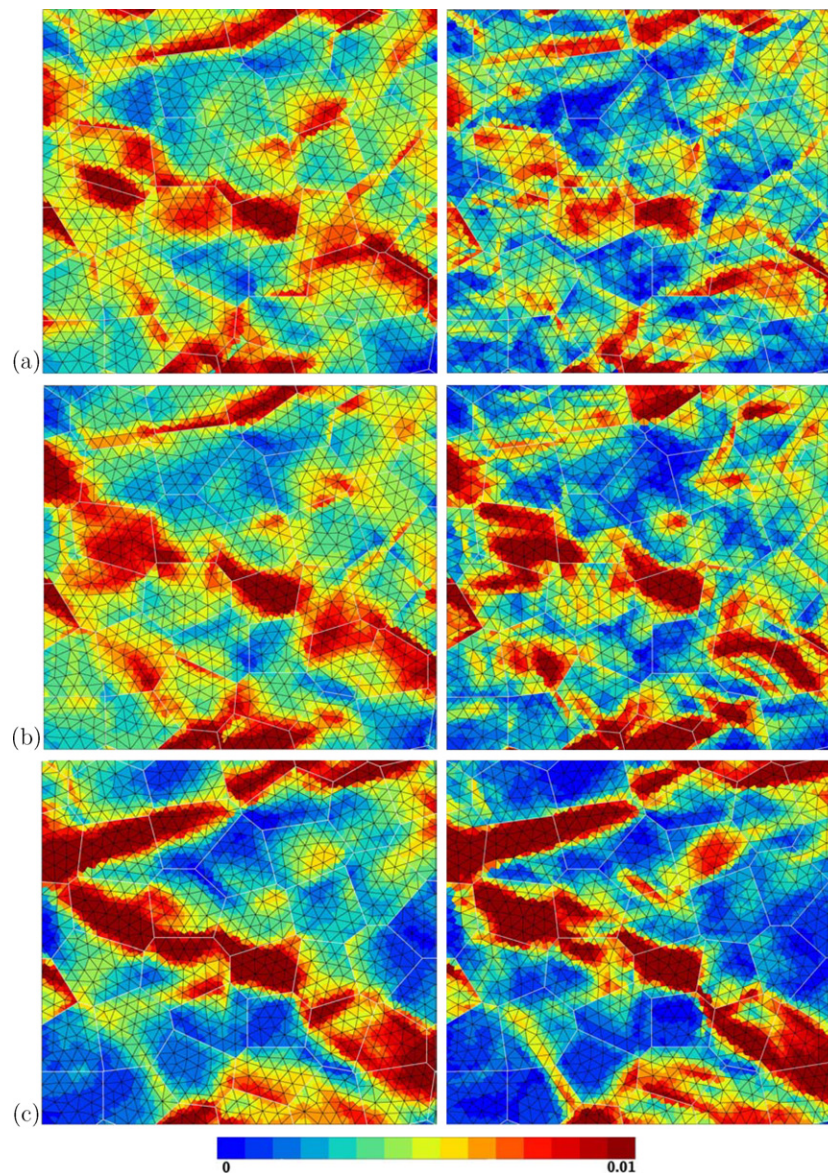


**Figure 11.** Distribution of equivalent plastic strain after  $N = 1$  cycle (left) and  $N = 100$  cycles (right): (a) multocrystalline film on a substrate with  $d/h = 1$ , (b) multocrystalline film on a substrate  $d/h = 0.5$ , (c) free-standing film.

histograms are computed, one for each grain orientation group as shown in figure 12. The evolution of the histograms can be characterized by the position and height of the peak and also by the range of the values. For all film configurations, texture component and loading conditions, the relative plastic strain values range from 0 to 5. The peak values, relative equivalent strain at peak and the width at half maximum are given in table 2 for the  $\{111\}$  grains. For increasing cycle number, the peak value and peak strain decrease whereas the width at half maximum increases. This last feature clearly shows that the distribution broadens with cycling, i.e. that dispersion of plastic strain increases. An additional clue for that is that, after

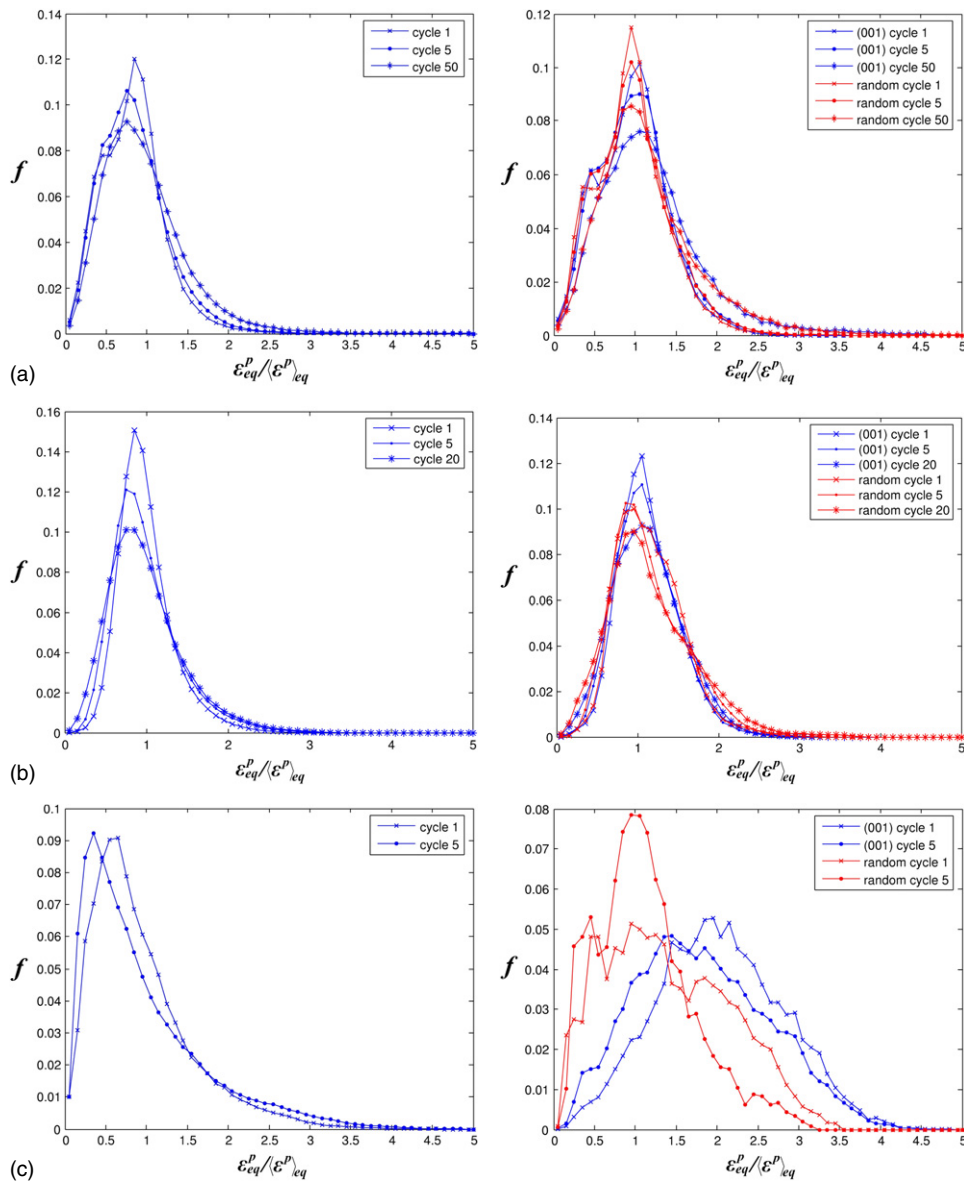


**Figure 12.** Histograms of equivalent plastic strain distribution after 1, 5 and 50 cycles in  $\{111\}$  grains (left) and  $\{001\}$  and random grains (right): (a) multicrystalline aggregate on a substrate with  $d/h = 1$ , (b) multicrystalline aggregate on a substrate with  $d/h = 0.5$ , (c) free-standing films. The results are based on the values found at all integration points in 10 aggregates for each film configuration ((a), (b), (c)). Strain values were distributed in classes with  $\Delta(\varepsilon_{eq}^p / \langle \varepsilon_{22}^p \rangle) = 0.1$ .

50 cycles, there are 6 times more points with relative plastic strain values higher than 1.7 than for the first cycle. This holds true for films on a substrate. The plastic strain distribution in free-standing films is significantly smaller and does not spread with cycling. This is due to a stronger tendency to strain localization so that strain develops in the same grains and cannot extend to neighbouring harder grains, as shown in figure 11(c). Note also that width at half maximum is smaller in columnar grains on a substrate than in equiaxial grains. The columnar

**Table 2.** Peak value, peak strain and width at half maximum in the relative equivalent plastic strain distribution in the  $\{111\}$  grains in three film configurations under cyclic tension-compression.

Cycle	Peak value	Peak strain	FWHM
Film with substrate ( $d/h = 1$ )			
Cycle 1	0.120	0.8	0.853
Cycle 5	0.106	0.7	0.946
Cycle 50	0.093	0.7	1.019
Film with substrate ( $d/h = 0.5$ )			
Cycle 1	0.151	0.8	0.570
Cycle 5	0.121	0.7	0.709
Cycle 20	0.101	0.7	0.872
Free-standing film			
Cycle 1	0.091	0.6	0.813
Cycle 5	0.092	0.3	0.713

**Table 3.** Identification of statistical distribution functions for the relative equivalent plastic strain in  $\{111\}$  grains for different film configurations under cyclic tension-compression.

Cycle	Lognormal	Weibull	Gamma
Film with substrate ( $d/h = 1$ )			
Cycle 1	$\mu = 0.2, \sigma = 0.45$	$k = 3.0, \lambda = 0.95$	—
Cycle 5	$\mu = 0.2, \sigma = 0.51$	$k = 2.4, \lambda = 0.90$	$\alpha = 4.0, \beta = 4.8$
Cycle 50	$\mu = 0.1, \sigma = 0.55$	$k = 2.2, \lambda = 1.0$	$\alpha = 4.7, \beta = 4.8$
Film with substrate ( $d/h = 0.5$ )			
Cycle 1	$\mu = 0.1, \sigma = 0.35$	—	—
Cycle 5	$\mu = 0.1, \sigma = 0.39$	—	—
Cycle 20	$\mu = 0.1, \sigma = 0.48$	—	$\alpha = 4.8, \beta = 5.1$
Free-standing film			
Cycle 1	$\mu = 0.2, \sigma = 0.65$	—	—
Cycle 5	$\mu = 0.25, \sigma = 0.70$	—	—

grains are more constrained and they cannot deform as easily as equiaxial ones. The dispersion of the plastic strain is then smaller than in the case of equiaxial grains.

The response of  $\{001\}$  grains displays even higher dispersions with cycling. Maximal range of classes increases from 2.7 to 5. The peak strain is 1.1 and remains almost unchanged during loading. The peak value decreases by about 20%. A similar behaviour is observed in random grains.

Analytical distributions have been fitted to the found histograms. The Lognormal, Weibull and Gamma distributions seem to be relevant:

$$f(x) = \frac{1}{x\sigma\sqrt{2\pi}} \exp\left(-\frac{(\ln(x) + \mu)^2}{2\sigma^2}\right), \quad f(x) = \left(\frac{k}{\lambda}\right) \left(\frac{x}{\lambda}\right)^{k-1} \exp\left(-\left(\frac{x}{\lambda}\right)^k\right),$$

$$f(x) = \frac{\beta^\alpha}{\Gamma(\alpha)} x^{\alpha-1} \exp(-\beta x). \quad (10)$$

The found parameters are given in table 3. The common feature of these distributions is that they lead to asymmetric histograms, which is a characteristic of the found plastic strain distribution. This is in contrast to the quasi-Gaussian distributions found in infinitely long columnar grains studied numerically in [9].

#### 4. Plasticity induced roughness

Heterogeneous plastic deformation is known to induce roughness at the free surface in films and coating [5, 23, 24]. Starting from an initially ideal plane surface in the simulation, the

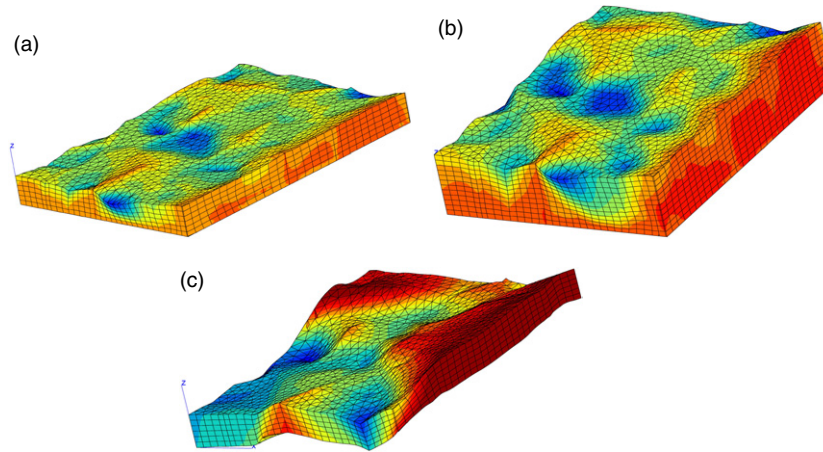


**Figure 13.** Deformed state of a multicrystalline aggregate for  $N = 100$ : (a) film on a substrate with  $d/h = 1$ , (b) film on a substrate with  $d/h = 0.5$ , (c) free-standing film. The grain morphology and orientation are the same in the three simulations. The considered field variable is the displacement component  $U_3$ . For the illustration, displacements have been magnified by a factor of 50.

crystal plasticity model provides estimates of plasticity induced roughness. The purpose of this section is to quantify the obtained roughness and its evolution during cycling loading.

#### 4.1. Definition of roughness parameters

Plasticity induced roughness is due to the 3D character of glide processes and the grain to grain strain incompatibility, which produces non-homogeneous out of plane displacement. Figure 13 shows the map of out of plane displacement  $U_3$  for the same aggregate placed in all three film configurations. Displacements are shown after 100 cycles with a magnification of 50 for the illustration. The constraining effect of the flat interface can be clearly seen in figures 13(a) and (b) compared with free-standing film (c). In the figure, blue grains correspond to a sink on the surface and red zones to a rise. Several thin and acute mountains can be seen, that coincide with grain boundaries, especially in the films on a substrate.

The absolute roughness  $R_{\text{RMS}}$  or root mean square roughness and the relative roughness  $R$  of the free surface are defined as

$$R_{\text{RMS}} = \sqrt{\frac{1}{n} \sum_{i=1}^n (U_3(x^i, y^i) - \bar{U}_3(x^i, y^i))^2}, \quad R = \frac{R_{\text{RMS}}}{|\langle \bar{U}_3 \rangle|}. \quad (11)$$

where  $U_3(x^i, y^i)$  is the displacement component of the given surface node  $(x^i, y^i)$  with respect to its initial position,  $\bar{U}_3(x^i, y^i)$  is the displacement of the average plane at the given position. The average plane is obtained by linear regression of the values of displacement using the least square method. The relative roughness  $R$  is obtained by normalizing  $R_{\text{RMS}}$  by the average displacement value  $\langle \bar{U}_3 \rangle$ . The previous definitions are valid for a sufficiently high number  $n$  of uniformly distributed points on the surface. Here the chosen points ( $n = 4000$  in average) are the finite element nodes at the free surface, the distribution of which is almost uniform.

A local relative roughness parameter can be defined at each point  $(x^i, y^i)$  of the free surface by

$$R_{\text{loc}}(x^i, y^i) = \frac{U_3(x^i, y^i) - \bar{U}_3(x^i, y^i)}{|\langle \bar{U}_3(x^i, y^i) \rangle|}. \quad (12)$$

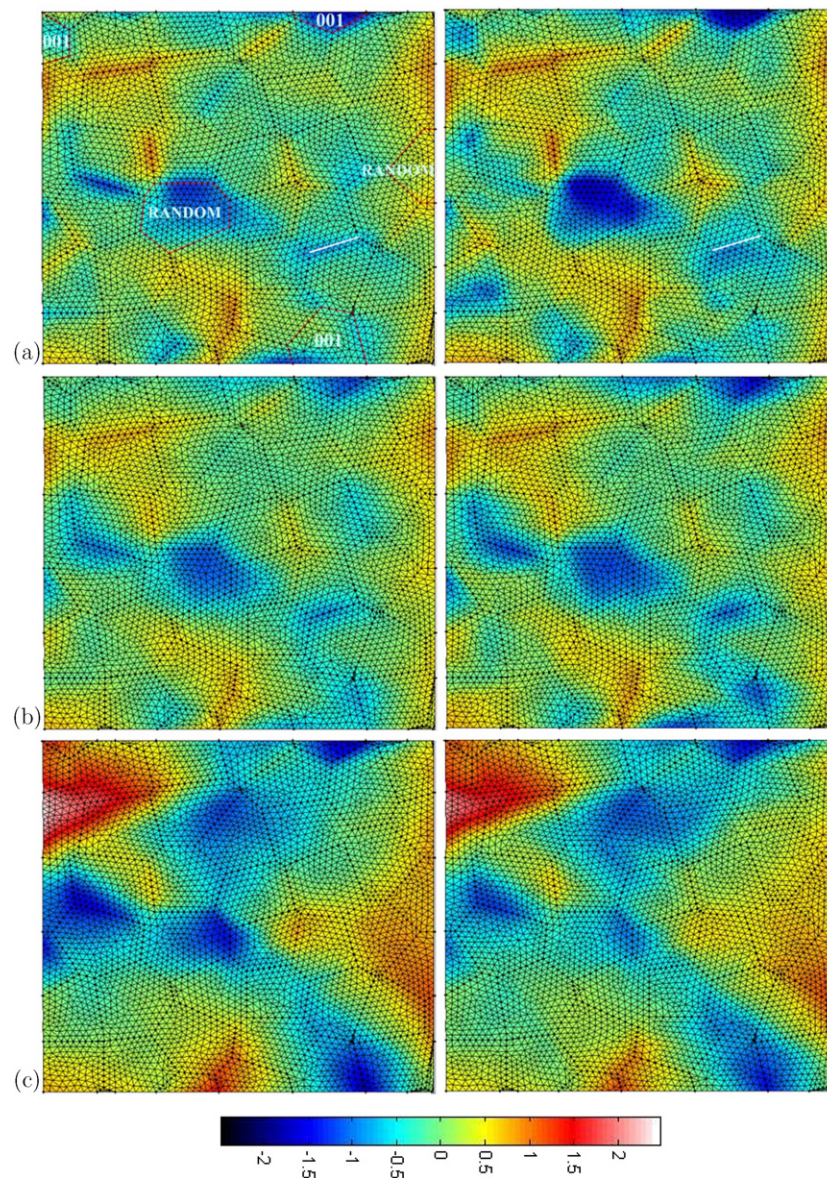


**Figure 14.** Roughness maps  $R_{10c}$  after  $N = 1$  (left) and  $N = 100$  (right) at maximal overall strain: (a) film on a substrate with  $d/h = 1$ , (b) film on a substrate with  $d/h = 0.5$ , (c) free-standing film.

#### 4.2. Results

The evolution of local relative roughness for the different film configurations at different cycles is shown in figure 14. The relative roughness is found to vary between  $-120\%$  and  $+120\%$  in films with a substrate and between  $-200\%$  and  $200\%$  in a free-standing film. The comparison of the maps at the first and 100th cycle shows that the absolute value of  $R_{10c}$  increases during cycling: sinking grains have a tendency to sink even more, rising grain boundaries rise even more after 100 cycles. The grain boundaries are superimposed on the mesh to confirm that

rising regions are mainly located at grain boundaries in the case of films on a substrate.

The analysis of plastic strain in differently oriented grains in section 3.2 has shown that the  $\{001\}$  and random grains on a substrate are significantly more deformed than  $\{111\}$  grains. This plastic deformation induces also higher roughness in these grains compared with the  $\{111\}$  ones. To show that, the  $\{001\}$  and random grains are indicated in figure 14(a) on the left. For comparison, in the experimental works [2, 3], higher amounts of extrusions were observed in the grains  $\{001\}$ , which caused higher roughening of the surface.

The evolution of global roughness  $R$  is given in figure 15 as a function of cycle number, for the three film configurations and both loading conditions and for all computed realizations. Roughness is computed at the maximal prescribed strain level. Global roughness is found to saturate after about 10 cycles which is early when compared with the saturation of cyclic hardening shown in figure 9. The dispersion in the asymptotic roughness associated with the different realizations is about 25% of the mean. The highest roughness is found for free-standing films. The roughness for tension-compression loading is higher than for the cyclic tension even though the prescribed maximal deformation is smaller.

The roughness amplitude, defined as  $|U_3^{\max} - U_3^{\min}|$  at a given time, is of the order of magnitude 1/100 of the film thickness in our simulations. This value is ten times smaller than the values measured in experiments [2, 3]. Two reasons can be put forward to explain this feature. First the experimental results were obtained after 10 000 cycles in contrast to the 100 cycles simulated in the present work. Secondly, roughness measured in the experiments is related to the height of the extrusions. These extrusions are related to the movement of dislocations. In the thin films with thickness of about  $1 \mu\text{m}$  these extrusions are created by dislocation events such as reactions of individual dislocations and multiple sources activation [2]. In the thicker films ( $100 \mu\text{m}$ ) these extrusions are associated with the formation of persistent slip bands [3]. The proposed continuum crystal plasticity framework is not able to predict transition in the damage mechanism, leading to extrusions and intrusions, without or with PSB formation. Such bands may well be triggered at a lower scale than that accounted for by the model. Recent simulations based on dislocation dynamics in a single grain plead for such a discrete modelling of dislocation reactions [25] and PSB [26].

An important result of the computations is the fact that roughness is mainly observed at grain boundaries that sink or rise. This is due to the high strain incompatibilities between neighbouring grains. This feature can be compared with the experimental observations and simplified model presented in [27]. The authors indicate that grain boundary rising or sinking is the predominant mechanism responsible for roughness development in some aluminium alloys during metal forming. In their observations, the emergence of slip lines, not accounted for in our simulations, played a lesser role in the roughening process. The proposed continuum crystal plasticity framework is indeed best suited for the interpretation of such experimental evidence. Quantitative comparisons remain to be drawn.

Saturation of global roughness does not mean that the local roughness does not evolve any longer. We have found evidence of ratcheting phenomena at certain locations on the free surface in the aggregates. Such a situation is illustrated in figure 16 where the local roughness is plotted along the grain boundary overlined in white in figure 14(a) for  $N = 50, 70, 100$  and  $N = 300$ . An increase in the local roughness at several positions of the grain boundary is observed from  $N = 70$  to  $N = 100$  although both the overall stress-strain loop and the global roughness are already saturated. The simulation of higher numbers of cycles up to 300 cycles shows that ratcheting phenomena tend to saturate, except at some nodes. A continuing ratcheting effect may be the precursor of fatigue strain accumulation and possible damage initiation.

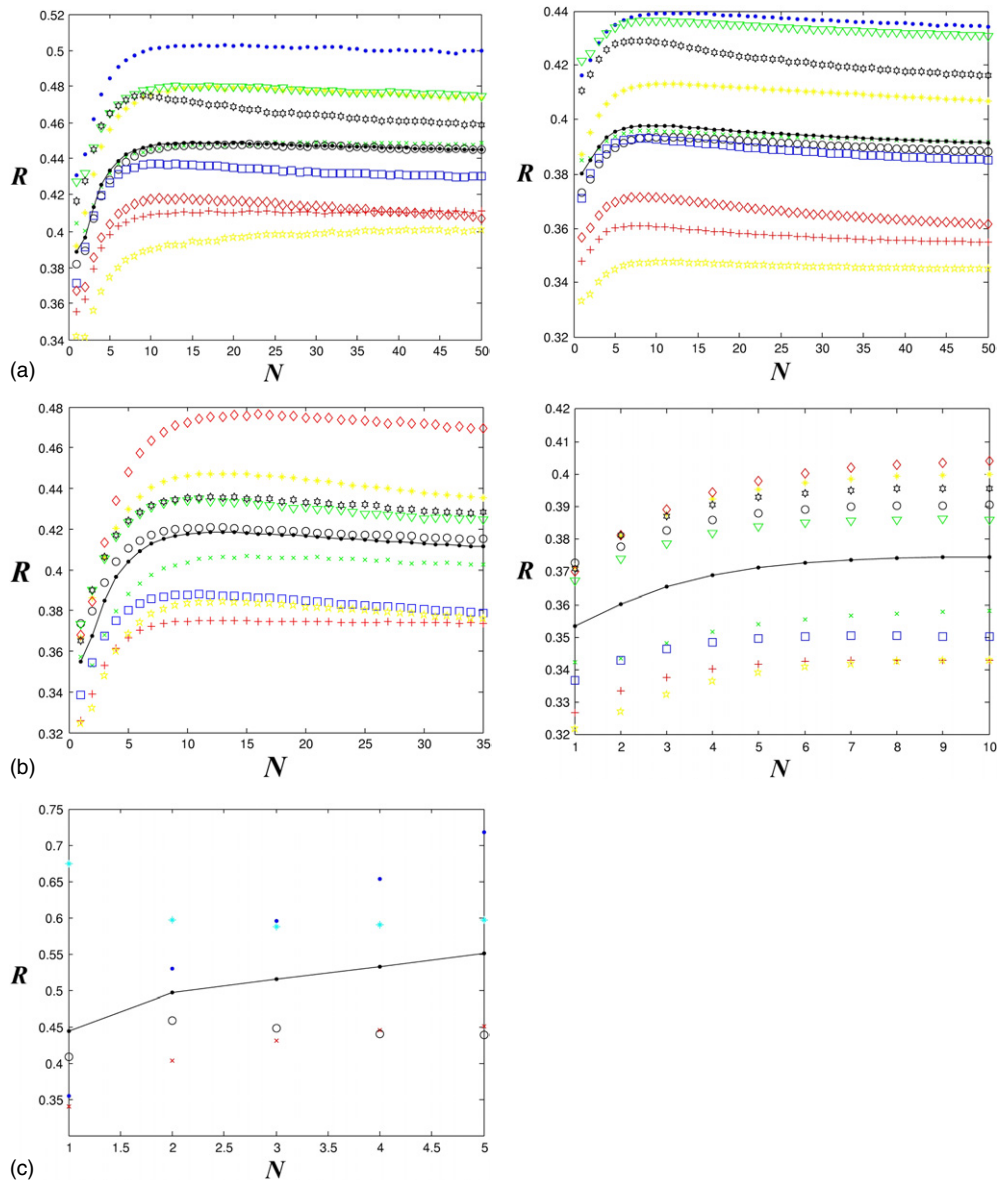


**Figure 15.** Evolution of global roughness with the number of cycles during cyclic tension-compression (left) and cyclic tension (right): (a) film on a substrate with  $d/h = 1$ , (b) film on a substrate with  $d/h = 0.5$ , (c) free-standing film. The results are plotted for all considered realizations, the black curve corresponds to the mean value.

### 5. Conclusions

A large-scale computational and statistical strategy has been undertaken to investigate the development of strain heterogeneities and free surface roughness in multicrystalline films on a substrate subjected to cyclic loading conditions, based on continuum crystal plasticity. For comparison, the case of free-standing films was also tackled. The main results are the

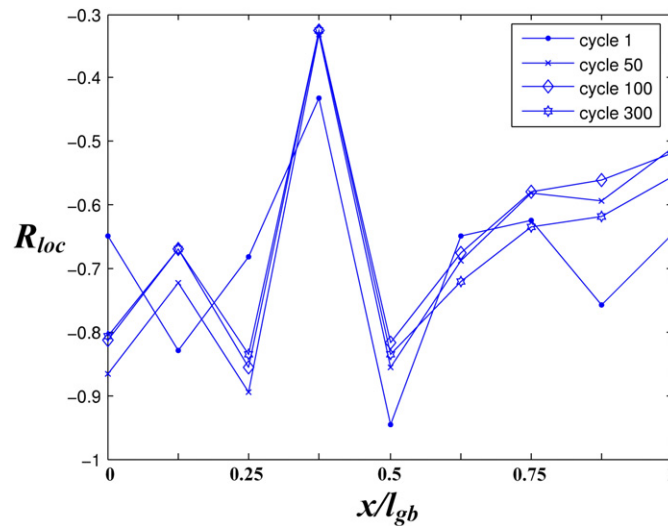


**Figure 16.** Evolution of local roughness along a selected grain boundary at the free surface. This grain boundary is marked by a white line in figure 14(a) on the left. Its total length is  $l_{gb}$ .

following:

- (i) Saturation of overall stress–strain loops towards the same limit cycle is observed in cyclic tension–compression and cyclic tension after about 70 cycles for films on a substrate. Significant overall kinematic hardening of the films is obtained, which is due to both intergranular interaction and local back-stress component introduced in the crystal plasticity model.
- (ii) A large dispersion in plastic strain distribution is observed in all film configurations with plastic strain concentration factors ranging from 0 to 500%. This dispersion is shown to increase significantly during cycling in films on a substrate but not in free-standing films.
- (iii) Higher deformation levels and dispersion are found in the  $\{001\}$  and random grains than in  $\{111\}$  grains, which is in accordance with experimental results provided in [2, 3].
- (iv) The plastic strain distributions are found to be asymmetric in all films with peak decreasing and distribution broadening in films on a substrate during cycling.
- (v) Plasticity induced roughness is shown to develop due to strain incompatibilities from grain to grain. The global relative roughness is found to saturate within 10 cycles at values in the range 40–50% in films on a substrate and towards higher values in free-standing films.
- (vi) Higher roughness levels are found to develop during cyclic tension–compression than during pure cyclic tension for the same strain amplitude and same limit cycle.
- (vii) The rising and sinking of grain boundaries in films on a substrate is observed at many places. This is the preferential location where local ratcheting phenomena can be observed.

The values of roughness amplitude found in this work are ten times smaller than in the experimental results provided in [2, 3]. This may be due to the too small amount of computed cycles, namely 100 against 10 000 in the experiment or to the impossibility of simulating the formation of persistent slip bands within the proposed continuum crystal plasticity framework. However the roughness computed in this work is an important estimate since plasticity induced roughness at the grain scale has strong consequences on the aspect of coatings on metal sheets for instance and for subsequent possible spalling [5, 23, 24]. The computations presented in

this work should also be analysed regarding stress and strain concentrations at the interface in order to estimate possible damage which is shown to occur at interfaces in [2, 3]. This may however require a proper meshing of the interface to take the local grain/substrate interaction into account.

An important limitation of the constitutive model used in this work is the crude description of local kinematic hardening. Indeed, kinematic hardening at the material point is the result of the building up of dislocation structures. If these structures are associated with local increased densities of GNDs (like in dislocation pile-ups), the kinematic hardening component can be related to such GND densities [18]. However, other structures can develop in cyclic deformation that are not associated with GNDs. The phenomenological equations used in this work combine in fact both aspects and are therefore limited in their prediction capacity. This is surely one part of the explanation for the deviation of the numerical results from experimental results regarding plasticity induced roughness. Improvements of the continuum material description is expected from simulations based on generalized continuum approaches as advocated in [14].

### Acknowledgment

Financial support for this project from European Commissions Human Potential Programme SizeDepEn under contract number MRTN-CT-2003-504634 is gratefully acknowledged.

### References

- [1] Hommel M and Kraft O 2001 Deformation behaviour of thin copper films on deformable substrates *Acta Mater.* **49** 3935–47
- [2] Schwaiger R, Dehm G and Kraft O 2003 Cyclic deformation of polycrystalline Cu films *Phil. Mag.* **83** 693–710
- [3] Schwaiger R and Kraft O 2003 Size effects in the fatigue behaviour in thin Ag films *Acta Mater.* **51** 195–206
- [4] Bhattacharyya A, El-danaf E, Kalidindi SR and Doherty RD 2001 Evolution of grain-scale microstructure during large strain simple compression of polycrystalline aluminium with quasi columnar grains: OIM measurements and numerical simulations *Acta Mater.* **17** 861–83
- [5] Parisot R, Forest S, Pineau A, Grillon F, Démonet X and Maitigne J-M 2004 Deformation and damage mechanisms of zinc coatings on galvanized steel sheets: I. Deformation Modes *Metall. Mater. Transac. A* **35** 797–811
- [6] Wilkström A and Nygård M 2002 Anisotropy and texture in thin copper films—an elastoplastic analysis *Acta Mater.* **50** 857–70
- [7] Cuitiño A M and Ortiz M 1993 Computational modelling of single crystals *Modelling Simul. Mater. Sci. Eng.* **1** 225–63
- [8] Barbe F, Decker L, Jeulin D and Cailletaud G 2001 Intergranular and intragranular behaviour of polycrystalline aggregates: 1. FE model. *Int. J. Plast.* **17** 513–36
- [9] Sai K, Cailletaud G and Forest S 2006 Micro-mechanical modeling of the inelastic behaviour of directionally solidified materials *Mech. Mater.* **38** 203–17
- [10] Šiška F, Forest S and Gumbsch P 2006 Simulation of stress–strain heterogeneities in copper thin films: texture and substrate effects *Comput. Mater. Sci.* at press
- [11] Parisot R, Forest S, Gourgues A-F, Pineau A and Mareuse D 2001 Modeling the mechanical behaviour of a multicrystalline zinc coating on a hot-dip galvanized steel sheet *Comput. Mater. Sci.* **19** 189–204
- [12] Weygand D, Brechet Y and Lepinoux J 1998 A vertex dynamics simulation of grain growth in two dimensions *Phil. Mag. B* **78** 329–52
- [13] Musienko A 2005 Large deformation and damage in crystal plasticity *PhD Thesis*, Ecole des Mines de Paris
- [14] Forest S, Barbe F and Cailletaud G 2000 Cosserat modelling of size effects in the mechanical behaviour of polycrystals and multiphase materials *Int. J. Solids Struct.* **37** 7105–26
- [15] Méric L, Poubanne P and Cailletaud G 1991 Single crystal modeling for structural calculations: 1. Model presentation *J. Eng. Mater. Technol.* **113** 162–70
- [16] Méric L, Cailletaud G and Gasperini M 1994 FE calculations of copper bicrystal specimens submitted to tension-compression tests *Acta Metall. Mater.* **42** 921–35

- [17] Tanaka K and Mura T 1981 A dislocation model for fatigue crack initiation *J. Appl. Mech.* **48** 97–103
- [18] Groma I, Csikor F F and Zaiser M 2003 Spatial correlations and higher-order gradient terms in a continuum description of dislocation dynamics *Acta Mater.* **51** 1271–81
- [19] Kawasaki Y and Takeuchi T 1980 Cell structures in copper single crystals deformed in the [00 1] and [1 1 1] axes *Scr. Metall.* **14** 183–8
- [20] Kozlov E V, Zhdanov A N, Popova N A, Pekarskaya E E and Koneva N A 2004 Subgrain structure and internal stress fields in UFG materials: problem of Hall–Petch relation *Mater. Sci. Eng. A* **387–9** 789–94
- [21] Kanit T, Forest S, Galliet I, Mounoury V and Jeulin D 2003 Determination of the size of the representative volume element for random composites: statistical and numerical approach *Int. J. Solids Struct.* **40** 3647–79
- [22] Cailletaud G 1992 A micromechanical approach to inelastic behaviour of metals *Int. J. Plast.* **8** 55–73
- [23] Raabe D, Sachtleber M, Weiland H, Scheele G and Zhao Z 2003 Grain-scale micromechanics of polycrystal surfaces during plastic straining *Acta Mater.* **51** 1539–60
- [24] Sachtleber M, Raabe D and Weiland H 2004 Surface roughening and color changes of coated aluminium sheets during plastic straining *J. Mater. Process. Technol.* **148** 68–76
- [25] Weygand D and Gumbsch P 2005 Study of dislocation reactions and rearrangements under different loading conditions *Mater. Sci. Eng. A* **400–401** 158–61
- [26] Déprés C, Robertson C F and Fivel M C 2004 Crack initiation in fatigue: experiments and three-dimensional dislocation simulations *Mater. Sci. Eng. A* **387–389** 288–91
- [27] Wilson W R D and Lee W 2001 Mechanics of surface roughening in metal forming processes *J. Manuf. Sci. Eng.* **123** 279–83